Materials and Design 168 (2019) 107644

Contents lists available at ScienceDirect

Materials and Design

journal homepage: www.elsevier.com/locate/matdes

Probabilistic neural network identification of an alloy for direct laser deposition

B.D. Conduit[a], T. Illston[b], S. Baker[b], D. Vadegadde Duggappa[c], S. Harding[d], H.J. Stone[e], G.J. Conduit[f,*]

[a] Rolls-Royce plc, Derby, PO Box 31DE24 8BJ, United Kingdom
[b] Materials Solutions, Worcester, WR4 9GN, United Kingdom
[c] Rolls-Royce India Private Limited, Manyata Tech Park, Bangalore 560024, India
[d] Rolls-Royce plc, Bristol, PO Box 3, BS34 7QE, United Kingdom
[e] Department of Materials Science & Metallurgy, University of Cambridge, 27 Charles Babbage Road, Cambridge CB3 0FS, United Kingdom
[f] Cavendish Laboratory, University of Cambridge, J.J. Thomson Avenue, Cambridge CB3 0HE, United Kingdom

HIGHLIGHTS

- Concurrent materials design with machine learning
- Exploit property-property relations
- Nickel-base alloy made by direct laser deposition
- Experimentally verified to be superior to alloys including C263 and CM247LC

GRAPHICAL ABSTRACT

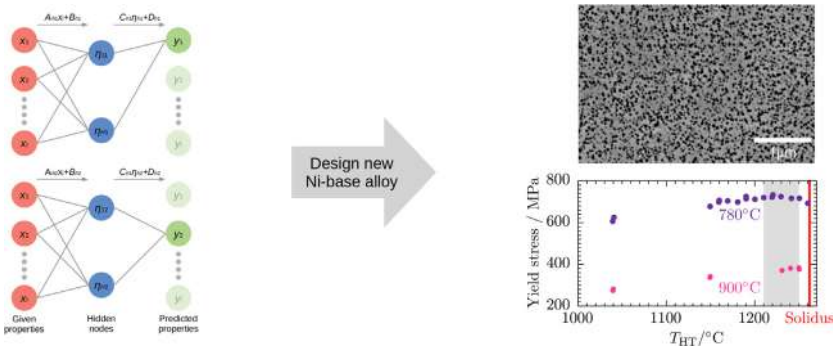

ARTICLE INFO

Article history:
Received 12 November 2018
Received in revised form 11 January 2019
Accepted 8 February 2019
Available online 21 February 2019

Keywords:
Nickel
Direct laser deposition
Alloy
Neural network

ABSTRACT

A neural network tool was used to discover a new nickel-base alloy for direct laser deposition most likely to satisfy targets of processability, cost, density, phase stability, creep resistance, oxidation, fatigue life, and resistance to thermal stresses. The neural network tool can learn property-property relationships, which allows it to use a large database of thermal resistance measurements to guide the extrapolation of just ten data entries of alloy processability. The tool was used to propose a new alloy, and experimental testing confirms that the physical properties of the proposed alloy are better tailored to the target application than other available commercial alloys.

1. Introduction

Direct laser deposition promises to accelerate the manufacturing process so that new components can go from drawing board to reality in a matter of hours. However, for this process to realize its full potential a new generation of materials are required that can accommodate the high temperature and stress gradients generated during this unique manufacturing process. Contemporary approaches to the development of new materials remains a lengthy process of experiment-driven trial and improvement [1]. There is therefore a significant opportunity to develop an approach to design bespoke alloys on the same timescales opened up by new

* Corresponding author.
E-mail address: gjc29@cam.ac.uk (G. Conduit).

https://doi.org/10.1016/j.matdes.2019.107644

manufacturing methods [2]. Such alloy design is particularly challenging as direct laser deposition has previously been applied to only around ten alloy compositions, restricting the volume of training data available. To this end, we have adopted a neural network driven approach [3–5] that can link data sets to allow the design of a new direct laser deposition alloy, and experimentally verify that the physical properties conform to the neural network predictions.

In designing an alloy that is suitable for this process, there are many material properties that need to be optimized simultaneously. Previous approaches to understand the compromise that must be made between different materials properties include ranking compositions with a Pareto set [6–8], characterizing materials with a principal component analysis [9], robust design [10], and the orthogonal optimization of different properties [2,11–14]. Neural networks [3–5,15–21], are a rapidly developing approach to capture deep composition-property correlations, however contemporary approaches do not explicitly capture the property-property correlations that will improve the quality of predictions. Furthermore, there are correlations between experimental results and computational tools, for example the CALPHAD approach to thermodynamics [22], PrecipiCalc [23,24], and Dictra [22]. These are useful tools to predict both the phases present and moreover their evolution. As such, when designing an alloy for direct laser deposition it is desirable to merge all of the data available, and in particular use the large data sets for CALPHAD thermodynamics to guide the extrapolation of the smaller data sets e.g. the processability for direct laser deposition; this requires the ability to establish property-property relationships. Therefore, we have developed a neural network tool [3–5] that can learn both composition-property and also property-property relationships to propose a new Ni-base alloy for use in direct laser deposition that is most likely to satisfy simultaneously the target properties of processability, cost, density, phase stability, creep resistance, oxidation, fatigue life, and resistance to thermal stresses.

Ni-base alloy are widely used in applications that demand good mechanical properties at high temperature alongside environmental resistance. The combustor liner in a gas turbine engine is a classic example, being exposed to temperatures of up to 950 °C and appreciable mechanical stresses. Nickel-base alloys presently used in combustor liner applications include HastealloyX, Haynes 282, Haynes 618, C263, and CM247LC. However, the combustor liner is a component whose complex geometric design would benefit from manufacture by direct laser deposition. The alloys C263 and CM247LC have previously been trialed for direct laser deposition so we adopt these as benchmarks. The effective design of an alloy for direct laser deposition requires an understanding of the relationship that exists between the alloy composition, the heat treatment schedule, processability, cost, density, phase stability, creep resistance, oxidation, and resistance to thermal stresses. This is a multidimensional problem for which we have developed a neural network-based formalism to analyze property-property relationships to guide extrapolation.

The first section of this paper outlines the neural network tool and specifies the chosen targets for the relevant material properties: processability, cost, density, phase stability, creep resistance, oxidation, and resistance to thermal stresses. In the second section, the tool is used to propose the composition and heat treatment regime (Table 2) for a new Alloy for Direct Laser Deposition, “AlloyDLD”. The final section presents experimental results for the phase stability, strength, ductility, oxidation, resistance to thermal stresses, and fatigue of the newly designed alloy to verify the model predictions.

2. Methodology

The goal of the neural network tool is to predict the composition and processing variables that are most likely to produce a material that fulfills the multi-criteria target specification. The tool and methodology is a development of the prescription in Refs. [3–5]. The tool comprises predictive models for each property as a function of the design variables, which for the Ni-base alloy presented contain the elements {Al, B, C, Co, Cr, Mo, Nb, Ni, W, Zr} and the heat treatment temperature. The neural network captures property-property correlations so it can use a property with a large amount of data to guide the extrapolation of another related property with sparse data. Critically, the tool can calculate the likelihood that a putative composition and heat treatment fulfills the target specification, so we search design space for the alloy most likely to meet the target specification.

2.1. Target specification

The goal is to design a new Ni-base alloy that offers both improved compatibility with direct laser deposition (more processable and giving a higher quality surface finish), and at the same time having superior high temperature mechanical properties than the current generation of Ni-base alloys that can be fabricated by direct laser deposition. As such, the alloy must fulfill a wide ranging specification, shown in Table 1, to ensure that it best meets the needs of the target application. The elemental cost should be below 25$kg^{-1} and the density should be below 8500kgm^{-3} to be competitive compared to other Ni-base alloys. Both cost and density are predicted using a model of the weighted commercial elemental prices and masses. The alloys with the most suitable mechanical properties are expected to be those that possess a Ni γ-phase containing up to only 25wt% of hardening γ' and minimal ($<$ 1.0wt%) amounts of other deleterious phases, giving two targets on the phase stability of the alloy. The thermodynamic phase stability is evaluated by a neural network trained on a database comprising of CALPHAD results, with data sourced from the TTNI8 database [22]. The use of a neural network to predict phase stability dramatically speeds up the alloy optimization process as it is computationally less intensive than individual thermodynamic calculations. We also require that the solvus temperature is $>$1000°C to be significantly above the envisaged highest use temperature of 950°C and to ensure that the strengthening γ' precipitates are retained in the microstructure during service. It is also essential for direct laser deposition alloys to be readily processable and, therefore, the fractional area density of cracks and pores must be minimized, set at $<$ 0.15% by area. To accommodate this, a thermal resistance parameter is defined as $\sigma_y/E\alpha\rho$ where, σ_y is the 0.2% proof stress, E the Young's modulus, α the thermal expansivity, and ρ the electrical resistivity, which correlates with thermal resistivity. To limit crack formation during processing, the alloy must have a good thermal resistance $>0.04K\Omega^{-1}m^{-1}$. To ensure good oxidation resistance we require a protective, well-adhered oxidation film giving a mass gain of less than 0.3 mg cm^{-2} at 950 °C for 100

Table 1
The table shows the approach used to predict properties, the number of experimental data entries used to train the neural network, and the references for the source of the data. The final column shows the targets for each material property.

Property	Approach	Entries	Target
Elemental cost	Physical	Model [25]	$<$ 25.0$kg^{-1}
Density	Physical	Model [26]	$<$ 8500kgm^{-3}
γ' content	CALPHAD	Model [22,27, 28]	$<$ 25wt%
Processability	Neural net	10 [29–33]	$<$ 0.15% defects
Oxidation resistance	Physical	Model [34]	$<$ 0.3 mg cm^{-2}
Phase stability	CALPHAD	Model [22,28]	$>$ 99.0wt%
γ'solvus	CALPHAD	Model [22,28]	$>$ 1000°C
Thermal resistance	Neural net	6939 [35–87]	$>$ 0.04KΩ^{-1}m^{-1}
Yield stress at 900°C	Neural net	6939 [35–87]	$>$ 200MPa
Tensile strength at 900°C	Neural net	6693 [35–87]	$>$ 300MPa
Tensile elongation at 700°C	Neural net	2248 [35–87]	$>$ 8%
1000hr stress rupture at 800°C	Neural net	10860 [35–87]	$>$ 100MPa
Fatigue life at 500 MPa, 700°C	Neural net	15105 [88,89]	$>$ 10^{5}cycles

Table 2
The composition of proposed material AlloyDLD (composition is in weight%) and the heat treatment. The design tolerance shows all design variables that are predicted to fulfill the target specification.

Optimal composition (wt%) and heat treatment			
Cr	19.0 ± 0.4	Co	4.0 ± 0.3
Nb	3.0 ± 0.1	W	1.2 ± 0.4
Mo	4.9 ± 0.2	Al	2.9 ± 0.2
C	0.04 ± 0.01	B	0.005 ± 0.002
Zr	0.045 ± 0.01	Ni	Balance
$T_{HT}/^{\circ}C$	1230 ± 20		

h. The alloy must also have good mechanical properties to be fit for service and, therefore, targets are set for the yield stress, tensile strength, tensile elongation, 1000 hour stress rupture, and the fatigue life that are enumerated in Table 1. The target for fatigue life was set to be similar to other commercially available alloys as we focus on improving other properties, particularly the processability. Many properties including all mechanical properties cannot be predicted reliably from first principles, so a database of experimental results for all of the properties as a function of composition and processing variables has been compiled from the sources referenced in Table 1. In the experimental validation we compare principally against the alloys C263 and CM247LC as these have previously been trialed for direct laser deposition.

2.2. Neural network formalism

With the individual property models and their associated targets, as specified in Table 1, we now turn to the neural network formalism. The design variables are the elemental concentration of {Al, B, C, Co, Cr, Mo, Nb, Ni, W, Zr} and the heat treatment temperature T_{HT}. However, for some properties there is little data available, in particular there are just ten entries for alloy processability stemming from alloys C263 [32], CM247LC [31], HastealloyX [29], Inconel718 [32], and Inconel738 [33]. We therefore develop a neural network formalism that can identify the link between processability, phase behavior, and other mechanical properties from common compositions and then use the surplus mechanical property data at other compositions to guide the extrapolation of the processability model. Only through this strategy is it possible to obtain meaningful predictions of without recourse to detailed knowledge of the mechanistic origins of such behavior. We first outline the feedback loop that allows the tool to complete missing endpoint data, before focusing in on the internal neural network kernel.

2.2.1. Handling incomplete data

Experimental data is often incomplete — not all properties are known for every alloy, and moreover the set of missing properties is different for each entry. However, there is information embedded within property-property relationships: in particular for direct laser deposition alloys the scarce processability data can be linked to the common thermal properties. A typical neural network formalism requires that each property is either an input or an output of the network, and all inputs must be provided to obtain a valid output. We treat all properties as both inputs and outputs of the neural network, but for a given composition we may know some properties but not others. We therefore develop a new neural network formalism based on an expectation-maximization algorithm [90], where we first provide an estimate for the missing data, and then use the neural network to iteratively improve that initial value.

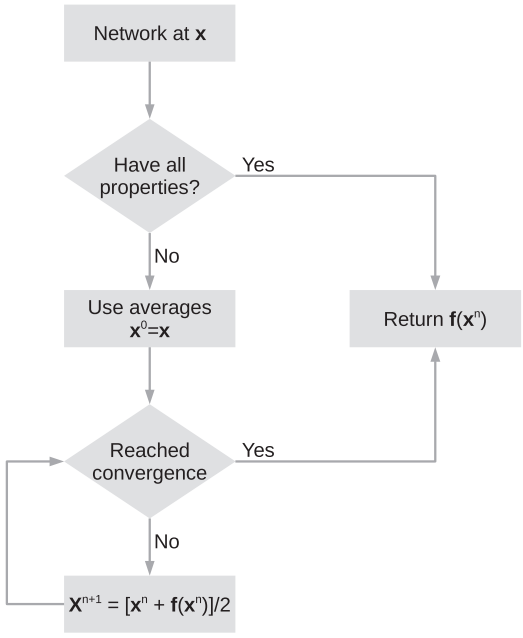

Fig. 1. The neural network for the vector **x** of the design variables and properties that has missing entries, computed recursively over n iterations.

The algorithm is shown in Fig. 1. For any unknown properties we first set missing values to the average of the values present in the data set. With estimates for all values of the neural network we can then iteratively compute

$$\boldsymbol{x}^{n+1} = \gamma \boldsymbol{x}^{n} + (1-\gamma)\boldsymbol{f}(\boldsymbol{x}^{n}) \,. \tag{1}$$

The converged result is then returned instead of $\mathbf{f}(x)$. We include a softening parameter $0 \leq \gamma \leq 1$, with $\gamma = 0$ ignoring the initial guess for the unknowns in **x** and determining them purely by applying **f** to those entries. However, $\gamma > 0$ will prevent oscillations of the sequence so we adopt $\gamma = 0.5$. Typically, 6 iteration cycles were used to fill in missing values. The benefits of the procedure to complete missing information will be seen when we perform cross-validation testing.

2.2.2. Neural network kernel

There are multiple forms of neural network. A feedforward neural network is the paradigmatic form that uses results from a previous layer to inform the next, a deep neural network can build up deep correlations. There are also more specialist capabilities for focused problem, for example a convolutional neural network is ideal for systems that display translational invariance and a recurrent neural network performs well on system that track time evolution. Here, due to the nature of the data, we adopt a feedforward neural network.

The neural network builds on the formalism used to design nickel-base superalloys, molybdenum alloys, and find errors in materials databases [3–5]. We seek a function f that satisfies the fixed-point equation $\mathbf{f}(\mathbf{x}) \equiv \mathbf{x}$ as closely as possible for all N elements **x** from the data set. Each entry $\mathbf{x} = (x_1, \ldots, x_I)$ is a vector of size I, and holds information about $I = 24$ distinct design variables and properties. The trivial solution to the fixed-point equation is the identity operator, but to impute data from other components we construct a solution to the fixed-point equation that is orthogonal to the identity operator.

The neural network is a linear superposition of hyperbolic tangents

$$\boldsymbol{f} : (x_1, \ldots, x_i, \ldots, x_I) \mapsto (y_1, \ldots, y_j, \ldots, y_I)$$
$$\text{with} \qquad y_j = \sum_{h=1}^{H} C_{hj}\eta_{hj} + D_j,$$
$$\text{and} \qquad \eta_{hj} = \tanh\left(\sum_{i=1}^{I} A_{ihj}x_i + B_{hj}\right). \qquad (2)$$

This neural network has a single layer of hidden nodes η_{hj} with parameters $\{A_{ihj}, B_{hj}, C_{hj}, D_j\}$ as shown in Fig. 2. Each property y_j for $1 \leq j \leq I$ is predicted separately. We set $A_{jhj} = 0$ so the network will predict y_j without the knowledge of x_j. Such a neural network can fully capture non-linear behavior, through the inclusion of the tanh function. This activation function typically outperforms others (including the rectified linear unit, logistic, and binary step) in quality of predictions by ~10% due the smoothness of the function and its derivative. The number of hidden nodes was selected by a five-fold cross-validation test [16,19,21]. Typically three hidden nodes gives the best fitting neural network. The weights were trained using a random walk to minimize the least-square error of its predictions against the training data. 10^7 training cycles were used to reach convergence. Twenty separate networks were trained on the data with different weights [3–5] and their variance taken to indicate the uncertainty in the predictions accounting for experimental uncertainty in the underlying data and the uncertainty in the extrapolation of the training data [91,92]. The neural network code is implemented in FORTRAN.

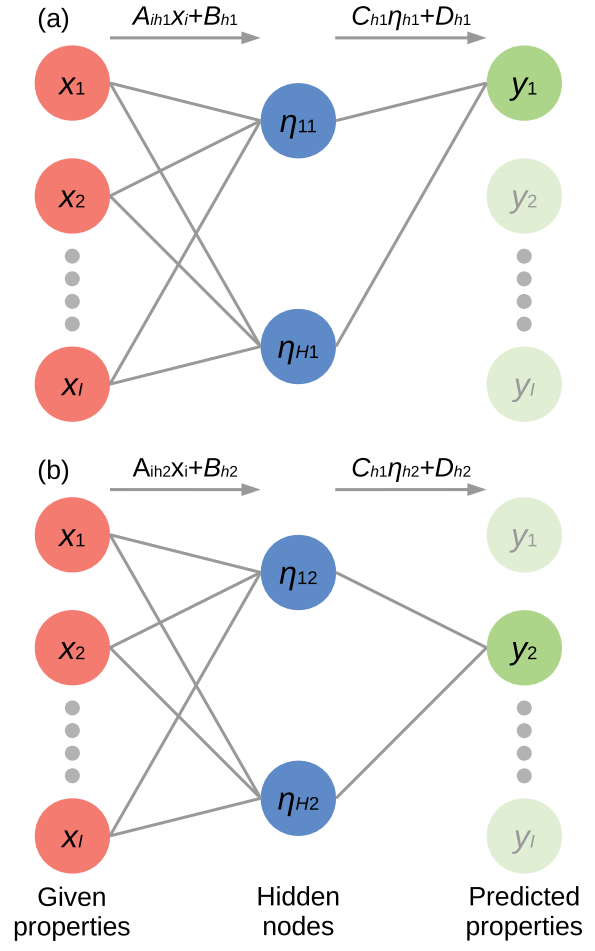

Fig. 2. The neural network. The graphs show how the outputs for y_1 (a) and y_2 (b) are computed from all the inputs. The given properties (red) are used to calculate the hidden nodes (blue) to give the predicted property (green). (For interpretation of the references to color in this figure legend, the reader is referred to the web version of this article.)

2.2.3. Cross-validation

To verify the accuracy of the neural network models cross-validation was performed. The network was trained on a randomly selected 80% of the data, and then validated against the remaining 20% of the data. The procedure was repeated five times on differently randomly selected data to give complete coverage of the entire data set. Cross-validation was performed on all properties, but in Fig. 3 (a), we highlight our results for the yield stress. The test was performed twice: first the neural network was trained on the data containing just the composition, heat treatment, and yield stress, and then the predictions for yield stress were compared with the validation data. Here, we find that the typical standard error in yield stress is 122 MPa. Next a neural network was trained on the data containing the composition, heat treatment, and all physical properties. This allowed it to learn property-property correlations (such as yield stress with tensile strength, stress rupture, and phase behavior) during training. This also enabled the neural network to learn about the complex composition-yield stress correlations by extrapolating based on related properties at other compositions.

During validation we provided the network with just the composition and heat treatment as inputs and the yield stress predictions are shown in Fig. 3 (a). We find that the typical standard error in yield

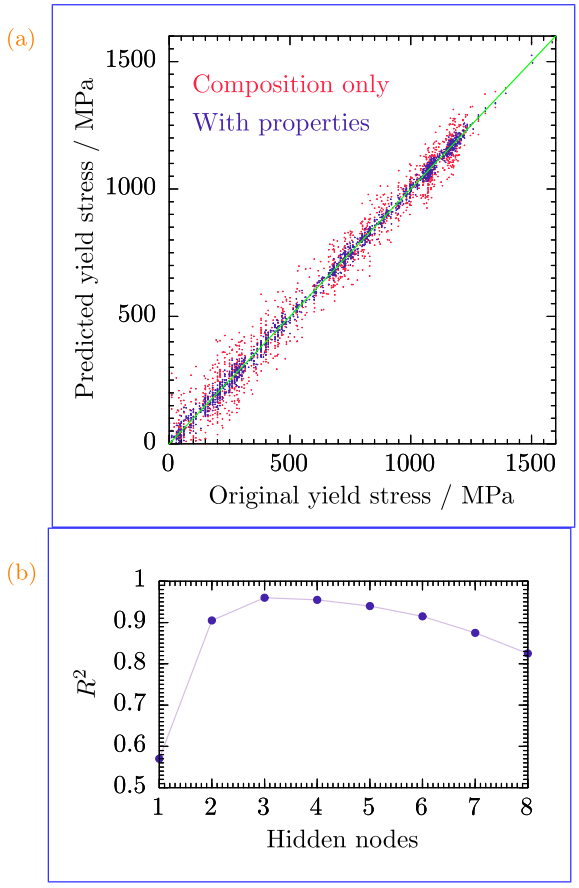

Fig. 3. (a) Cross-validation test for experimental yield stress (x-axis) with predicted yield stress (y-axis). The green line shows the expected result for a perfect prediction. The pink points show the yield stress predictions when trained with just composition and heat treatment information, the purple points show the predictions when trained with both composition and also other physical properties. b) Cross-validation test for yield stress with number of hidden nodes in the neural network.

stress is just 37 MPa, an improvement by over a factor of three. We follow Refs. [16,19,21] and adopt the coefficient of determination as a dimensionless measure for quality of fit, allowing us to compare and compute the fit for different quantities with different units. We achieve a coefficient of determination $R^2 = 0.96$. An additional test can be performed on the ability to extrapolate in chemical space. We split the data set into a training set of alloys with >1wt% of Aluminum and validated on those alloys with < 1wt% of Aluminum. We achieved a coefficient of determination $R^2 = 0.89$, confirming the ability to extrapolate into new chemical space.

A similar level of accuracy is achieved during cross-validation testing for other physical properties with an average coefficient of determination $R^2 = 0.95$. The lowest three properties with the lowest coefficient of determination were processability with $R^2 = 0.83$, tensile elongation with $R^2 = 0.86$, and tensile strength with $R^2 = 0.92$, which are also the properties with the fewest data points. On the other hand cost, and density were both perfectly modeled with $R^2 > 0.995$. Finally, we also tested placing the commercially available C263 and 100 nearest materials in composition space into a validation data set. The properties of these materials could be predicted with $R^2 = 0.94$, confirming the ability to extrapolate in composition space and ultimately design new materials.

Cross-validation was also used to verify the number of hidden nodes adopted. In Fig. 3 (b), we study the how the coefficient of determination for fitting the yield stress data changes with number of hidden nodes. With too few hidden nodes the fit is poor as the model cannot properly fit the data, and with too many hidden nodes the model over fits and accuracy falls. The optimal number if hidden nodes to fit the yield stress data is three.

Finally, the ability of the neural network to understand the uncertainty in its predictions was tested. Specifically, comparison was made between the standard error predicted by the neural network and the actual difference from unseen validation data, which on average should be unity. We find that the root mean square average ratio is 1.05 with standard deviation 0.12, confirming the ability of the neural network to understand the accuracy of its predictions.

2.3. Optimizing the material properties

In this approach, the individual material properties are converted into a single merit index $L = \Phi[\Sigma^{-1}(\vec{V} - \vec{T})]$ that describes the likelihood that the material properties ($\vec{V}$) satisfy the design criteria ($\vec{T}$). Here,Φ is the multivariate cumulative normal distribution function and Σ is the covariance matrix [93]. Combining the individual property likelihoods enables an estimate to be made of the likelihood that the alloy will fulfill the whole specification. Therefore, the use of likelihood also allows the tool to explore and select the ideal compromise between material properties, which is inaccessible with methods that do not account for likelihood, such as a principal component analysis [9] and robust design [10], and the neural network allows us to capture deeper correlations than linear regression methods such as in principal component analysis [9].

As well as predicting material properties, the tool must vary the composition and processing variables to optimize the properties against the set targets. Previous optimization techniques included running over a predetermined grid of compositions, and then sieving them with trade-off diagrams [13], or a Pareto set [6–8]. However the expense of these methods scales exponentially with the number of design variables. Another approach is to use genetic algorithms [94,95], but this approach is not mathematically guaranteed to find the optimal solution [96,97] and it displays poor performance in high dimensional problems [96,97]. Here, we maximize the logarithm of the likelihood $\log(L)$ to ensure that in the region where the material is predicted to not satisfy the specification the optimizer runs up a constant gradient slope that persistently favors the least optimized property. The tool searched high-dimensional composition space with bounds on elemental composition of $5\% \leq Cr \leq 30\%$, $0 \leq \{Nb,Mo,Co,W,Al\} \leq 8\%$, $0 \leq \{C,Zr,B\} \leq 1\%$, and processing variable $900^{\circ}C \leq T_{HT} \leq 1300^{\circ}C$, taken from the limits of the training data. We explore the design space with a random walk that uses a step length comparable to the accuracy with which a material could be manufactured. This is 0.1 wt% for the entire composition excluding the possibility of microsegregation. The tool typically search over $\sim 10^8$ sets of design variables in ~1 h to explore the space and search for an optimal material.

2.4. Alloy proposed

With the neural network tool established, a new Ni-base alloy was designed to fulfill the targets in Table 1, and the properties of the alloy subsequently verified by experiment. The neural network proposed the composition and processing variables for AlloyDLD, shown in Table 2. This alloy is predicted to have a 30% likelihood of meeting the target specification. The composition is quoted with a range of concentrations that were predicted to satisfy all of the target criteria. AlloyDLD notably has high levels of Cr, at 19 wt %, and no Ti to ensure good oxidation resistance. However, inevitably, the neural network code must make a compromise between the different properties of an alloy. This can be directly visualized from the predicted properties and an example is shown in Fig. 4, which illustrates the probability of fulfilling the design criteria as the targets for thermal resistance and phase stability are changed. The probability is zero in the top-left hand corner of the graph at low phase stability and high thermal resistance denotes the physical impossibility of an alloy existing with these properties as the targets for thermal resistance and phase stability are too ambitious. The proposed alloy is the one most likely to fulfill the targets and is highlighted as it lies at the center of the largest region of highest likelihood. The rapidly varying likelihood of satisfying all of the targets reflects how other properties change markedly. This variation is similar to that seen in the design of other Ni-base superalloys [3] and Mo-base alloys [4]. The understanding of this landscape of likelihood also allows an engineer to select the ideal compromise for their application, for example with the aid of an Ashby plot [98].

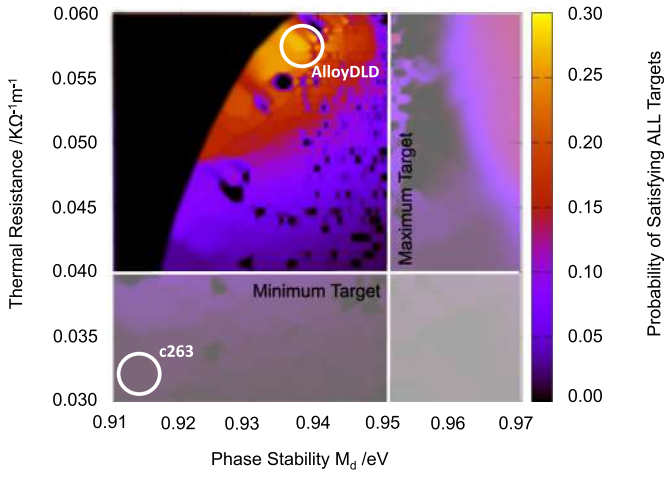

Fig. 4. The probability of an alloy fulfilling the design criteria as the targets for the thermal resistance (y-axis) and phase stability (x-axis) are varied. The white shaded areas show regions that fail to meet thermal resistance and phase stability targets. The color of shading shows the likelihood of exceeding all of the targets, following the scale on the right. The white circles show the proposed AlloyDLD and existing alloy C263. (For interpretation of the references to color in this figure legend, the reader is referred to the web version of this article.)

3. Manufacture

The proposed AlloyDLD is predicted to fulfill the target specification. However, experiments are required to verify its performance. A 30 kg ingot of AlloyDLD was prepared by vacuum induction melting. This was then subjected to gas atomization and then sieved to produce a powder with a particle distribution that varied between 10 and 100μm, with a mean value of 30μm. Test pieces were manufactured using direct laser deposition with a range of energy densities, scan speed, and scan spacing combined into an "exposure parameter".

To measure the area fraction of defects shown in Fig. 7, extensive micro-structural analysis was carried out on selected samples using scanning electron microscopy (SEM). Samples were analyzed in their horizontal and vertical planes, parallel and perpendicular to the build plane respectively. Using the exposure parameter with the lowest area fraction of defects, sample blanks were built for property testing. The samples were solution heat treated at 1230 °C (for 2 h) followed by a precipitate heat treatment (20 h at 800 °C).

4. Results

The experimental properties of AlloyDLD were assessed in two stages: first the physical properties of AlloyDLD were studied and compared to other alloys including CM247LC, and C263. Secondly, the effect of varying the heat treatment temperature, T_{HT}, on the properties of AlloyDLD were studied to confirm that the optimal processing variables had been selected.

4.1. Physical properties

Fig. 6 (a) shows a secondary electron micrograph of AlloyDLD. The presence of a γ matrix containing ~15% γ′ precipitates is consistent with the neural network prediction of ~17% γ′ phase. Three heat treatment tests at (700 °C, 800 °C, 900 °C) for 1000 h showed only slight γ′ phase evolution and no deleterious phases, confirming the phase stability. Fig. 6 (b) also shows a sample combustor liner formed by direct laser deposition out of AlloyDLD. The surface finish achieved is consistent with other alloys suitable for direct laser deposition; this is further evidence that AlloyDLD is suitable for direct laser deposition.

Oxidation properties were measured by preparing samples of the test alloys measuring 30 × 10 × 0.5 mm, with a 4000 grit surface finish. For each sample, a hole was spark eroded and the sample was hung on a fine mass balance that can weigh to an accuracy of 0.015 mg. The sample was exposed to an area of the furnace where the temperature was measured to be 950 ± 2° C and the mass change of the sample was then recorded every 60 s, or every 0.12 mg mass change for a duration of 100 h. In Fig. 5 (a), it can be observed that the mass gain matches well with the neural network prediction, improves on CM247LC and is significantly better than C263. This confirms that AlloyDLD fulfills the target specification of having good oxidation resistance.

The thermal resistance was calculated as a function of temperature for both horizontally and vertically built samples, and the results obtained are compared with the neural network prediction in Fig. 5 (b). This was achieved by measuring properties defined in the thermal resistance parameter separately. The properties are similar for the horizontally and vertically printed samples, confirming good material homogeneity. The neural network predictions for the thermal resistance of C263 match well with the experimentally measured values, and moreover the neural network predictions for AlloyDLD agree well with experiment. We note that for AlloyDLD the experimental prediction at 900 °C has slightly lower thermal resistance than predicted by the neural network. However, it is only slightly more than one standard deviation out (where 30% of measurements

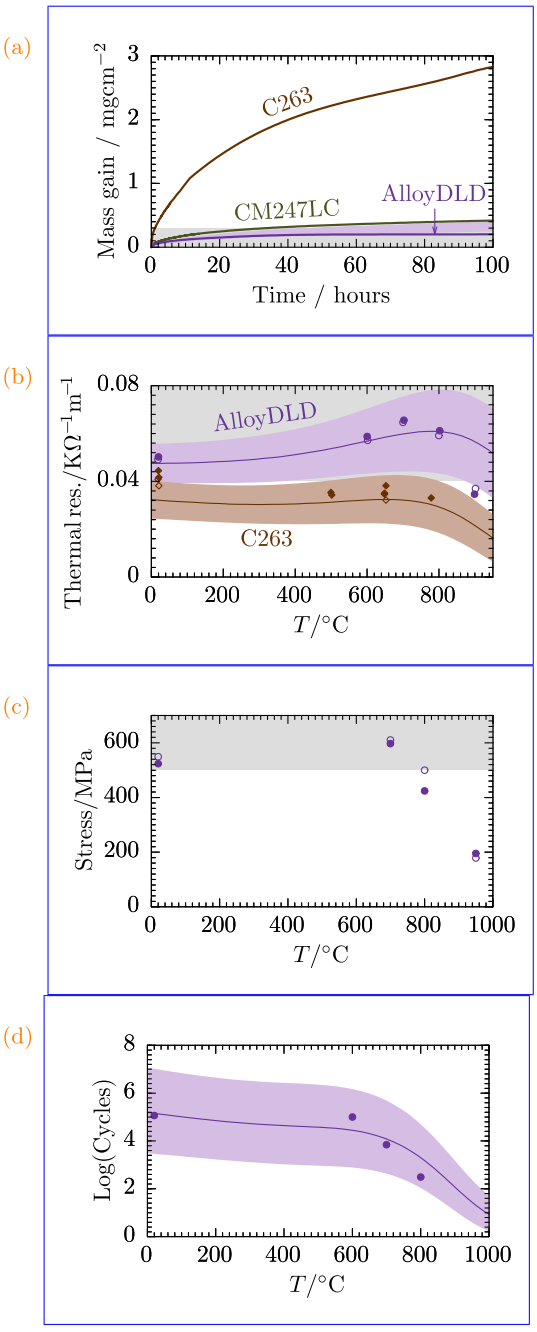

Fig. 5. (a) The thick lines show the mass gain at 950°C with time of the AlloyDLD, CM247LC, and C263. The shaded purple area denotes the range of neural network predictions for the mass gain of AlloyDLD. (b) The points show the thermal resistance of samples of AlloyDLD and C263 printed horizontally (solid circle and diamond points respectively) and vertically (open circle and diamond points respectively). The neural network predictions are shown by the solid lines with uncertainty denoted by the shaded region. (c) The 10^5 cycle fatigue stress with temperature for AlloyDLD printed horizontally (solid circle points) and vertically (open circle points). (d) The low cycle fatigue cycles with temperature for AlloyDLD printed horizontally. In all graphs the gray shaded region denotes the target range. (For interpretation of the references to color in this figure legend, the reader is referred to the web version of this article.)

are expected to be), and this is at the upper bound of temperatures that the model can be applied at, where its predictions can be expected to be less accurate. The experimental results confirm that AlloyDLD has a higher thermal resistance than C263. For CM247LC, the mechanical properties and thermal resistance cannot be meaningfully compared because it is difficult to process using direct laser

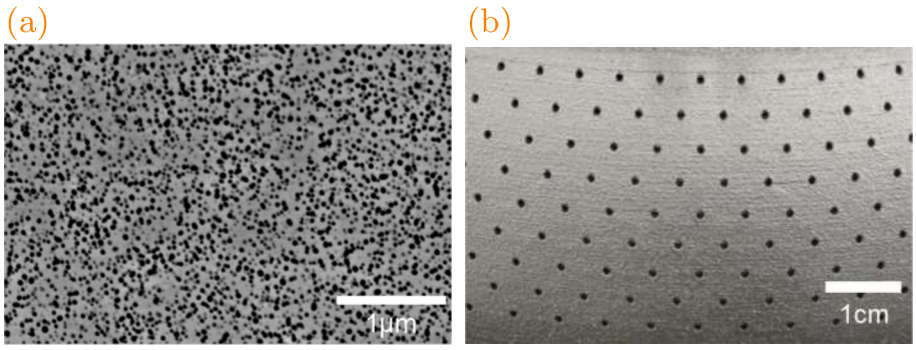

Fig. 6. (a) Secondary electron micrograph image for AlloyDLD. (b) Representative geometry of a sample combustor manufactured by direct laser deposition.

deposition resulting in cracking throughout the alloy. This has been suggested due to residual stresses throughout the build process [99].

In Fig. 5 (c), we show the high (10^5) cycle fatigue for a machined sample of AlloyDLD between 0 and 500 MPa. The similarity of the results for horizontally and vertically printed samples show good homogeneity of the samples. In Fig. 5 (d), it can also be observed that for notched samples measured in load controlled fatigue at 600 MPa between room temperature and 800 °C the number of cycles to failure measured in experiment matches well with the theoretical prediction. To probe the creep resistance we measured the 1000 hour stress rupture at 800 °C for a sample printed in the horizontal direction, recording 105 MPa, surpassing the target of 100 MPa.

4.2. Defects

Sections of the assembled geometry were assessed using a scanning electron microscope to evaluate the area fraction of defects within the material. Fig. 7 (a) shows how the defect content of the material varied with the exposure parameter. A higher exposure parameter led to a lower area fraction of defects. From this it can be inferred that a lower scan spacing, scan speed, and energy density lead to a lower proportion of defects in the material. For an alloy that is subjected to three-dimensional loading it is important that the area fraction of defects shown in is kept to a minimum in both the horizontal and vertical directions so that the mechanical properties are not compromised. The area fraction of defects for horizontally and vertically printed samples is shown to have a similar correlation with the exposure parameter, showing that the area fraction of defects can be minimized to a low level.

4.3. Heat treatment

The samples were solution heat treated for 2 h followed by a precipitate heat treatment at 800°C for 20 h. To better understand the choice of solution heat treatment temperature, T_{HT}, the variation of ductility with T_{HT} is shown in Fig. 7 (b). The ductility was measured with the sample held at two different test temperatures: 780 °C and also 900 °C, it rises rapidly with T_{HT} to a plateau at an optimal value in the region of $T_{HT} = 1230 \pm 20^{\circ}$ C, as specified. It is not possible to increase T_{HT} above the solidus temperature of 1262 °C, so the heat treatment has been specified to be as near to the solidus as practically possible. Fig. 7 (c) also shows the variation of yield stress with solution temperature. This was measured on a machined test sample at a strain rate of $0.001 s^{-1}$ with a 15 minute dwell at the testing temperature. Here, the variation is smooth, but again shows that the selected solution temperature gives the optimal values for yield stress. AlloyDLD has a higher yield stress than C263 [72] at both test temperatures, confirming its real-life utility. The study confirms that the neural network has selected the optimal processing conditions for AlloyDLD.

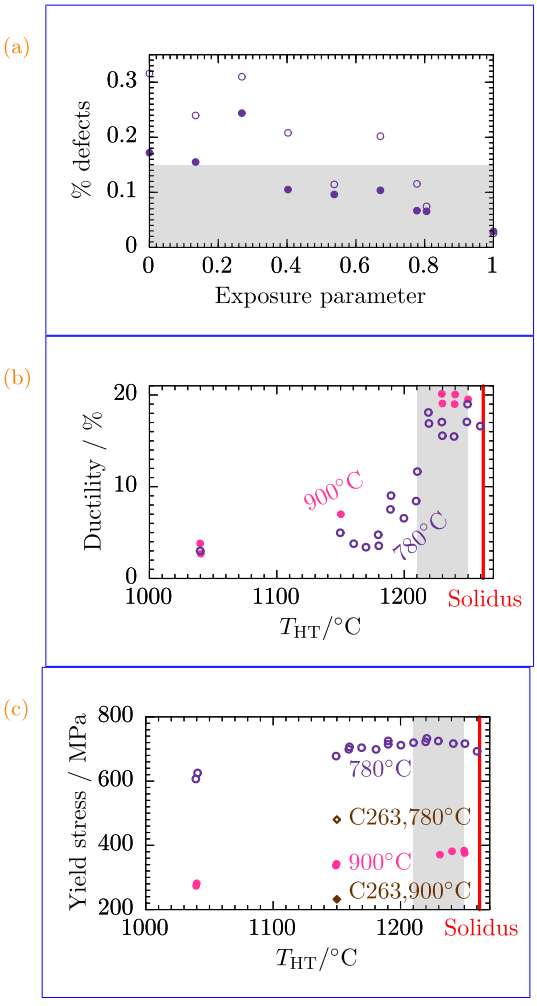

Fig. 7. (a) Area percentage of defects in the AlloyDLD with exposure parameter. The solid circles are for samples printed horizontally and the open circles are for samples printed vertically. The gray shaded region denotes the target range. (b) Elongation with heat treatment temperature measured at 780°C (open magenta circles) and 900°C (closed pink circles). (c) Yield stress with heat treatment temperature measured at 780°C (open magenta circles) and 900°C (closed pink circles). The gray shaded region denotes the range of recommended design heat treatment temperatures, and the red vertical line denotes the solidus temperature. We also show two results for C263 (open diamonds at 780°C and closed diamonds at 900°C). (For interpretation of the references to color in this figure legend, the reader is referred to the web version of this article.)

5. Conclusions

A neural network was used to propose the Ni-base AlloyDLD most likely to simultaneously fulfill thirteen physical criteria (processability, cost, density, phase stability, creep resistance, oxidation, fatigue life, and resistance to thermal stresses) given the experimental and computational data available. The neural network was guided in its extrapolation of ten data points for processability by using physical data for other properties. AlloyDLD has been experimentally verified to have phase behavior, processability, oxidation resistance, thermal resistance, yield stress, fatigue life, and ductility properties that match the neural network predictions and are better tailored to the target application than other available commercial alloys. With high levels of processability, oxidation resistance, thermal resistance, and good high-temperature mechanical properties, AlloyDLD possesses the properties to be used as a combustor liner manufactured by direct laser deposition.

The authors acknowledge the financial support of Rolls-Royce plc,EPSRC underEP/H022309/1 andEP/H500375/1, theRoyal Society, andGonville & Caius College. Copyright University of Cambridge. There is Open Access to this paper and data available at https://www.openaccess.cam.ac.uk.

CRediT authorship contribution statement

B.D. Conduit: Data curation, Formal analysis, Investigation, Software, Writing - original draft. **T. Illston:** Investigation, Validation. **S. Baker:** Investigation, Validation. **D. Vadegadde Duggappa:** Data curation, Formal analysis, Investigation. **S. Harding:** Conceptualization, Funding acquisition. **H.J. Stone:** Conceptualization, Funding acquisition, Project administration, Supervision, Writing - review & editing. **G.J. Conduit:** Conceptualization, Methodology, Investigation, Software, Writing - original draft.

References

[1] S. Curtarolo, G. Hart, M. Buongiorno Nardelli, N. Mingo, S. Sanvito, O. Levy, Nat. Mater. 12 (2013) 191.
[2] C. Kuehmann, G. Olson, Mater. Sci. Eng. 25 (2009) 472.
[3] B. Conduit, N. Jones, H. Stone, Mater. Des. 131 (2017) 358.
[4] B. Conduit, N. Jones, H. Stone, G. Conduit, Scr. Mater. 146 (2018) 82.
[5] P. Verpoort, P. MacDonald, G. Conduit, Comput. Mater. Sci. 147 (2018) 176.
[6] T. Bligaard, G. Jóhannesson, A. Ruban, H. Skriver, K. Jacobsen, J. Nørskov, Appl. Phys. Lett. 83 (2003) 4527.
[7] J. Greeley, T. Jaramillo, J. Bonde, I. Chorkendorff, J. Nørskov, Nat. Mater. 5 (2006) 909.
[8] K. Lejaeghere, S. Cottenier, V. Van Speybroeck, Phys. Rev. Lett. 111 (2013) 075501.
[9] I. Toda-Caraballo, E. Galindo-Nava, P. Rivera-Díaz-del Castillo, J. Alloys Compd. 566 (2013) 217.
[10] D. Backman, D. Wei, D. Whitis, M. Buczek, P. Finnigan, D. Gao, J. Mater. (2006) 3641.
[11] M. Joo, J. Ryu, H. Bhadeshia, Mater. Manuf. Process. 24 (2009) 5358.
[12] W. Xu, P. Rivera Diaz del Castillo, S. van der Zwaag, Comput. Mater. Sci. 45 (2009) 467.
[13] R. Reed, T. Tao, N. Warnken, Acta Mater. 57 (2009) 5898.
[14] F. Tancret, Modelling Simul. Mater. Sci. Eng. 21 (2013) 045013.
[15] W. Shaa, K. Edwards, Mater. Des. 28 (2007) 1747.
[16] G. Khalaj, Neural Comput. & Applic. 23 (2013) 779–786.
[17] G. Khalaj, A. Nazari, H. Pouraliakbar, Neural Network World 23 (2013) 117.
[18] G. Khalaj, H. Pouraliakbar, Ceram. Int. 40 (2014) 5515.
[19] M. Faizabadi, G. Khalaj, H. Hesam Pouraliakbar, M. Jandaghi, Neural Comput. & Applic. 25 (2014) 1993–1999.
[20] N. Narimani, B. Zarei, H. Pouraliakbar, G. Khalajd, Measurement 62 (2015) 97.
[21] H. Pouraliakbar, M.-J. Khalaj, M. Nazerfakhari, G. Khalaj, J. Iron Steel Res. Int. 22 (2015) 446.
[22] J. Andersson, T. Helander, L. Höglund, P. Shi, B. Sundman, Calphad 26 (2002) 273.
[23] J. Langer, A. Schwartz, Phys. Rev. A 21 (1980) 948.
[24] R. Kampmann, R. Wagner, Materials Science and Technology Phase Transformations in Materials, Wiley-VCH. 1991.
[25] American Elements, Element Catalogue, Available from. cited 2018 20 December. www.americanelements.com.
[26] R.C. Reed, T. Tao, N. Warnken, Acta Mater. 57 (2009) 5898.
[27] L. Connor, The Development of a Dual Microstructure Heat Treated Ni-Base Superalloy for Turbine Disc Applications,Ph.D. thesis. University of Cambridge. 2009.
[28] J. Bratberg, H. Mao, L. Kjellqvist, A. Engström, P. Mason, C. Q., Proceedings of the International Symposium on Superalloys 2012, Wiley. 2012, 803–812.
[29] L. Carter, M. Attallah, R. Reed, Superalloys 2012: 12th International Symposium on Superalloys, Wiley. 2012, p. 577.
[30] plc. Rolls-Royce, Rolls Royce Internal Data, Tech. Rep., Rolls-Royce plc. 2014.
[31] V. Divya, R. Muñoz-Moreno, O. Messé, J. Barnard, S. Baker, I. T., H. Stone, Mater. Sci. Technol. 114 (2016) 62.
[32] S. Yusuf, N. Gao, Mater. Sci. Technol. 33 (2017) 1269.
[33] A. Ramakrishnan, G. Dinda, Mater. Sci. Eng. A 740-741 (2019) 1.
[34] K. Christofidou, N. Jones, M. Hardy, H. Stone, Oxid. Met. 85 (2015) 443.
[35] C. Tomasello, F. Pettit, N. Birks, J. Maloney, J. Radavich, Superalloys, Miner. Met. Mater. Soc. 1996. 1996, 145–151.
[36] J. Radavich, D. Furrer, Superalloys, Miner. Met. Mater. Soc. 2004. 2004, 381–390.
[37] C. Sims, N. Stoloff, W. Hagel, Superalloys II, High Temperature Materials for Aerospace and Industrial Power, John Wiley & Sons, Inc. 1987.
[38] B. Ewing, F. Rizzo, C. ZurLippe, Superalloys 1972, 1972, 1.
[39] K. Sato, T. Ohno, J. Mater. Eng. Perform. 2 (1993) 511.
[40] S. Mannan, S. Patel, J. de Barbadillo, Superalloys, Miner. Met. Mater. Soc. 2000. 2000, 449–458.
[41] R. Mitchell, Development of a New Powder Processed Ni-Base Superalloy for Rotor Disc Application,Ph.D. Thesis. University of Cambridge. 2004.
[42] Z. Meng, G.-C. Sun, M.-L. Li, X. Xie, Superalloys 1984 (1984) 563.
[43] J. Tien, J. Collier, G. Vignoul, Superalloy 718 (1989) 553.
[44] E. Huron, K. Bain, D. Mourer, J. Schirra, P. Reynolds, E. Montero, Superalloys 2004, Miner. Met. Mater. Soc. (2004) 73–81.
[45] K. Sharma, S. Tewari, J. Mater. Sci. 18 (1983) 2915.
[46] C. Cowen, P. Jablonski, Superalloys 2008, Miner. Met. Mater. Soc. 2008, 201–208.
[47] L. Pike, Superalloys 2008, Miner. Met. Mater. Soc.2008, 191–199.
[48] S. Mannan, G. Smith, S. Patel, Superalloys, 2004, J. Miner. Met. Mater. Soc. 2004, pp. 627–635.
[49] D. Tillack, H. Eiselstein, Superalloys 718, 625 and Various Derivatives, Miner. Met. Mater. Soc.1991, 1–14.
[50] F. J., J. Radavich, Superalloys 718, 625 and Various Derivatives, Miner. Met. Mater. Soc.1991, 297–308.
[51] J. Moll, G.N. Maniar, D. Muzyka, Metall. Mater. Trans. B 2 (1971) 2153.
[52] J. Brinegar, J. Mihalisin, J. VanderSluis, Superalloys 1984 (1984) 53.
[53] G. Bouse, M. Behrendt, Superalloy 718 (1989) 319.
[54] A. Braun, J. Radavich, Superalloy 718 (1989) 623.
[55] C.K.M., A. Nahm, Superalloy 718 (1989) 631.
[56] L. Jackman, G. Smith, A. Dix, M. Lasonde, Superalloys 718, 625 and Various Derivatives, Miner. Met. Mater. Soc.1991, 125–132.
[57] J. Schirra, R. Caless, R. Hatala, Superalloys 718, 625 and Various Derivatives, Miner. Met. Mater. Soc.1991, 375–388.
[58] E. Guo, F. Xu, E. Loria, Superalloys 718, 625 and Various Derivatives, Miner. Met. Mater. Soc.1991, 397–408.
[59] S. Mannan, E. Hibner, B. Puckett, Physical Metallurgy of Alloys 718, 725, 725HS, 925 for Service in Aggressive Corrosive Environments, Tech. Rep., Special Metals. 2003.
[60] F. Rizzo, J. Buzzanell, Superalloys 1968 (1968) 501.
[61] J. Radavich, D. Meyers, Superalloys 1984 (1984) 347.
[62] X. Xie, X. Liu, Y. Hu, B. Tang, Z. Xu, J. Dong, K. Ni, Y. Zhu, S. Tien, L. Zhang, W. Xie, Superalloys, Miner. Met. Mater. Soc. 1996. 1996, 599–606.
[63] S. Loewenkamp, J. Radavich, Superalloys 1988 (1988) 53.
[64] P. Quested, M. Mclean, M. Winstone, Superalloys 1988 (1988) 387.
[65] D. Seib, Superalloys, Miner. Met. Mater. Soc. 2000. 2000, 535–544.
[66] S. Shaw, Superalloys, Miner. Met. Mater. Soc. 1980. 1980, 275–284.
[67] G. Sjoeberg, D. Imamovic, J. Gabel, O. Caballero, J. Brooks, J. Ferte, A. Lugan, Superalloys, Miner. Met. Mater. Soc. 2004. 2004, 441–450.
[68] M. Nganbe, M. Heilmaier, Int. J. Plast. 25 (2009) 822.
[69] M. Kaufman, Superalloys 1984 (1984) 43.
[70] R. Eng, D. Evans, Superalloys, Miner. Met. Mater. Soc. 1980. 1980, 491–500.
[71] J. Brinegar, L. Norris, L. Rozenberg, Superalloys 1984 (1984) 23.
[72] Special Metals, Nimonic alloy 263, Available from. cited 2018 20 December. www.specialmetals.com/assets/smc/documents/alloys/nimonic/nimonic-alloy-263.pdf.
[73] D. Locq, M. Marty, P. Caron, Superalloys, Miner. Met. Mater. Soc. 2000. 2000, 395–403.
[74] J. Barker, E. VanDerMolen, Superalloys 1972 (1972) 1.
[75] D. Hunt, The Stability & Mechanical Properties of a Nickel-Base Turbine Disc Alloy,Ph.D. thesis. Emmanuel College, University of Cambridge. 2001.
[76] E. Wanner, D. DeAntonio, Superalloys, Miner. Met. Mater. Soc. 1992. 1992, 237–246.
[77] J. Tien, J. Collier, P. Bretz, B. Hendrix, High temperature materials for power engineering, Chap. Raising the High Temperature Limit of IN718-Designing Ticolloy, Kluwer Academic Publishers. 1990, 1341–1348.
[78] Y. Gu, C. Cui, H. Harada, T. Fukuda, D. Ping, A. Mitsuhashi, K. Kato, T. Kobayashi, J. Fujioka, Superalloys, Miner. Met. Mater. Soc. 2008. 2008, 53–61.
[79] R. Couturier, H. Burlet, S. Terzi, S. Dubiez, L. Guetaz, G. Raisson, Superalloys, 2004, Miner. Met. Mater. Soc. 2004, pp. 351–359.

[80] F. Sczerzenie, G. Maurer, Superalloys 1984 (1984) 573.
[81] S. Jain, B. Ewing, C. Yin, Superalloys, Miner. Met. Mater. Soc. 2000. 2000, 785–794.
[82] K. Green, Superalloys, Miner. Met. Mater. Soc. 1996. 1996, 697–703.
[83] D. Furrer, H. Fecht, Superalloys, Miner. Met. Mater. Soc. 2000. 2000, 415–424.
[84] A. Ferrari, Superalloys 1976 (1976) 201.
[85] G. Raisson, Y. Honnorat, Superalloys 1976 (1976) 473.
[86] E. Richards, R. Cook, Superalloys 1968 (1968) 1.
[87] G. Maurer, L. Jackman, J. Domingue, Superalloys, 1980, Miner. Met. Mater. Soc. 1980, pp. 43–52.
[88] Special Metals, Available from. cited 2018 20 December. www.specialmetals.com.
[89] Haynes International Inc., Available from. cited 2018 20 December. www.haynesintl.com.
[90] T. Krishnan, G. McLachlan, The EM Algorithm and Extensions, Wiley. 2008.
[91] T. Heskes, Advances in Neural Information Processing Systems 9, MIT Press. 1997, pp. 176–182.
[92] G. Papadopoulos, P. Edwards, A. Murray, IEEE Trans. Neural Netw. 12 (2001) 1278.
[93] L. Wasserman, All of Statistics: A Concise Course in Statistical Inference, Springer. 2004.
[94] G. Jóhannesson, T. Bligaard, A. Ruban, H. Skriver, K. Jacobsen, J. Nørskov, Phys. Rev. Lett. 88 (2002) 255506.
[95] D. Stucke, V. Crespi, Nano Lett. 3 (2003) 1183.
[96] L. Ingber, B. Rosen, Mathl. Compat. Modelling 16 (1992) 87.
[97] S. Mahfoud, D. Goldberg, Parallel Comput. 21 (1995) 1.
[98] M. Ashby, Materials Selection in Mechanical Design, Burlington, Massachusetts: Butterworth-Heinemann. 1999.
[99] X. Wang, L. Carter, B. Pang, M. Attallah, M. Loretto, Acta Mater. 128 (2017) 87.